Detection of Transits of Extrasolar Giant Planets With Inexpensive Telescopes and CCDs

Timothy P. Castellano
NASA Ames Research Center, Astrophysics Branch, MS 245-6, Moffett Field, CA 94035

Gregory Laughlin
Richard Stone Terry
UCO/Lick Observatory, University of California, Santa Cruz, CA 95064

Michael Kaufman
Seth Hubbert
GionMatthias Schelbert
San Jose State University, Department of Physics, One Washington Square, San Jose, CA, 95192

Dorian Bohler
Randy Rhodes
National Association for Equal Opportunity in Higher Education, NASA Ames Research Academy, MS 19-48, Moffett Field, CA 94035

Received August 26, 2004; revised November 10, 2004; accepted November 10, 2004

Abstract A typical short-period giant planet occulting a parent star can produce a ~1% dimming of the star's light for an interval of several hours. The combination of photometric and Doppler radial velocity (RV) measurements of a transiting extrasolar planet can yield unambiguous measurements of the planet's mass, radius, density, and exact orbital parameters. In this article, we describe a low-cost observational and data-reduction pipeline which can be used to obtain 3 milli-magnitude photometry with a small-aperture telescope and a consumer-grade CCD detector. This precision is sufficient to reliably detect the transit of a giant planet. We discuss noise sources, and evaluate strategies for achieving a low overall noise floor. We describe the performance of our pipeline in a successful observation of an HD 209458 "b" transit, and in a photometric survey of GJ 876 during an epoch in which we predicted that GJ 876 "c" (P ~30d) could potentially be observed to transit. We also briefly describe the status of the ongoing www.transitsearch.org project, which coordinates a photometric search for planetary transits among known planet-bearing stars.

1. Introduction

The planetary companion to HD 209458 occults the stellar disk as seen from Earth every 3.52474541 ($\pm 2.5 \times 10^{-7}$) days (Wittenmyer *et al.* 2003) and during these

transits, the amount of light coming from the star is reduced by ~1.5% (Charbonneau *et al.* 2000; Henry *et al.* 2000). The transit phenomenon has allowed astronomers to conduct detailed follow-up measurements of HD 209458 "b", including determinations of the planet's radius ($1.35 \pm 0.06 R_{JUP}$ (Brown *et al.* 2001); $1.41 \pm 0.10 R_{JUP}$ (Cody and Sasselov 2002)), and mass ($0.69 \pm 0.05 M_{JUP}$; (Mazeh *et al.* 2000)). The discovery of a second transiting planet (OGLE TM-56-b; Konacki *et al.* 2003) has led to similar physical measurements ($R = 1.26 \pm 0.15 R_{JUP}$, $M = 1.4 \pm 0.2 M_{JUP}$). The parameters of OGLE TR-56-b have greater uncertainties, however, because the parent star is much dimmer: V=16.6 for OGLE TR-56, as compared to V=7.67 for HD 209458.

Many near-term advances in our understanding of giant planets, and indeed of planetary formation in general, will hinge on the discovery of additional planets that transit bright parent stars. A bright parent star permits both high-quality radial velocity measurements and also high quality photometric light curves. These complementary methods combine to reveal the orbital and physical properties of the transiting planet (for an overview, see Charbonneau 2004).

Photometric surveys for transiting extrasolar planets are well-suited for finding objects with periods of order P < 10d (see e.g. Pepper, Gould, and DePoy 2003) but have difficulty detecting longer-period transits due to the long time-baselines that are required. In a companion paper (Seagroves *et al.* 2003), we conducted Monte-Carlo studies that demonstrate a loosely coordinated network of small telescopes can effectively discover transiting planets of intermediate (10d < P < 200d) period by photometrically monitoring stars known to harbor planets from radial velocity surveys. The discovery of an intermediate-period transiting planet would be of great value, as it would effectively bridge the gap between high-temperature objects such as HD 209458 "b" and OGLE TR-56-b, and the familiar giant planets in our own solar system. Furthermore, an intermediate-period transiting planet orbiting a bright parent star can be followed up with high-precision photometry (with HST, for example, as described by Brown *et al.* 2001) to search for large, potentially habitable moons. Such a discovery is a long shot; however, it is tantalizing nonetheless.

If a straightforward observation and data reduction pipeline can be developed without requiring a large telescope or significant data reduction, a wider base of observers could participate in follow-up searches to detect transits. While achieving sub-1% photometry is not a trivial undertaking, it is nevertheless feasible with an 8-inch aperture telescope in a suburban setting at sea level using a commercially available CCD, and we are optimistic that the pool of potential observers might soon expand significantly.

2. Photometric precision and sampling requirements for the detection of extrasolar planets

The median expected transit depth among the extrasolar planets detected with the RV method and with periods in the range 10d < P < 200d, is 1.04% (Computed using data from http://www.ucolick.org/laugh/candidates.html). The predicted

transit depth, *d*, depends on both the planetary and the stellar radius. Within the current catalogue of planets, and assuming Jupiter radii, *d* ranges from *d* = 0.01% for the planet orbiting the large radius G type giant star HD 104985 to *d* = 13.8% for the planet orbiting the small radius M type dwarf star GJ 876. A reasonable precision goal for a search effort capable of detecting most of the potential transits might thus be 1 to 3 milli-magnitudes for all noise sources combined.

The required maximum photometric sampling interval is determined by transit durations that generally last several hours. For a circular orbit about a $1\ M_{\odot}$ primary, the transit duration, t_d, of a planet with semi-major axis, *a*, is $t_d = 13(\sqrt{a\ /\ 1AU})$ hr, indicating a weak $t_d\ \alpha\ P^{1/3}$ dependance of transit duration on orbital period. In order to be convincing, the photometric cadence must be high enough for either the planetary ingress or egress (which each extend for approximately 1/10 to 1/6 of the transit duration) to be well sampled. Since a Jupiter radius planet is roughly 1/10 the size of solar radius star ingress and egress are 1/10 of the transit duration. For a planet like HD 209458 "b" that is 1.35 Jupiter radii ingress and egress can be somewhat longer and extend to approximately 1/6 of the transit duration. Systematic errors can easily produce trends in photometric data due to image motion or changes in air mass over a night's observing (see the following sections), but the relatively rapid changes in brightness that occur as the planet crosses the stellar limb should dominate on shorter timescales. Furthermore, Poisson statistics indicate that the significance of a transit detection increases in proportion to $N^{1/2}$, where *N* is the number of independent photometric samples within the transit interval.

Differential photometry—the measurement of the difference in brightness between two or more stars—is well-suited to the detection of planetary transits. Differential photometry (see Henden and Kaitchuk 1990 for an overview) requires no reduction to magnitude systems tied to standard stars. If the stars to be compared are near one another on the celestial sphere and are similar in color, or if observations are limited to small values of air mass, the first-order (air mass difference dependent only) extinction and the second-order (color difference dependent) extinction corrections are generally small compared to the expected photometric transit depth. Furthermore, CCD differential photometry allows the simultaneous measurement of the brightness of all stars in a given field through virtually identical values of airmass.

Small differences in airmass across the field of view can be well-modeled by applying corrections for first-order and second-order extinction. Differential CCD photometry has been demonstrated to achieve precision as low as 0.0008 magnitude for a 9-hour time series with 2-minute cadence on a 1-meter class telescope (Gilliland *et al.* 1991). Differential photometry is largely unaffected by small changes in atmospheric transparency such as light clouds. The first-order extinction is given by $v_o = v - a_v \times X$ where v_o is the true extinction-corrected apparent magnitude, *X* is the airmass, a_v is the *V*-band first-order extinction coefficient in magnitudes per unit airmass, and v is the measured *V*-band magnitude. Second-order extinction depends on the color difference between the target star and a comparison star, and

is defined by $v_o = \upsilon - a_v \times X - b_v \times (B-V) \times X$. Here, b_v is the second-order extinction coefficient in units of magnitudes per airmass per unit difference in $B-V$ color in magnitudes.

A significant difficulty posed for photometric follow-up surveys concerns the lack of bright comparison stars in the field of view (FOV). High precision RV surveys for extrasolar planets require target stars with $V < 10$ to obtain both maximum efficiency and 3 to 5 ms^{-1} precision. There are 225,300 stars in the *Henry Draper Catalogue*, which is nearly complete to V = 9.5, hence there are approximately 5 stars brighter than 10th magnitude per square degree. The suitably bright comparison stars required for standard stellar differential photometry are, therefore, often lacking within a CCD FOV of even a telescope of moderate aperture and focal length. Spot filter photometry is one way to overcome this limitation (Castellano 2000). Small apertures are also an advantage, and a focal reducer can inexpensively expand the FOV by a factor of two or more. Focal reducers do, however, have the drawback of concentrating more of the light from a star in fewer pixels which can limit exposure times and even lead to undersampled images for the best seeing conditions. The expected FOV for a small commercially available telescope with a CCD and a focal reducer (such as the system described later) is about 0.25 deg^2 . This FOV size is unrivaled by large telescopes unless they are equipped with mosaic imagers. However, mosaic imagers are both expensive and slow to read out.

3. Sources of noise

To achieve milli-magnitude photometric precision (a worthy and challenging goal for a small telescope of perhaps 20 centimeters in aperture with an inexpensive CCD) one must exert great care to minimize random noise sources. These sources include: 1) Poisson noise from the target and comparison stars, 2) noise introduced during calibration, 3) noise deriving from atmospheric scintillation, and 4) CCD read noise. We consider in turn the effect of each of these sources on a typical low-cost Telescope-CCD combination.

3.1. Poisson noise

In order to achieve milli-magnitude precision, the measured stellar variability arising from Poisson noise, σ, must be smaller than one part in a thousand. Poisson statistics dictate that $\sigma = 1/\sqrt{N}$, where N is the number of photo-electrons collected in the alotted stellar aperture, indicating that more than 10^6 photo-electrons are required for both the object star and at least one comparison star. For a $V = 7.67$ magnitude star such as HD 209458, Figure 1 shows that a small telescope meets this requirement with an exposure time $t < 10$s.

3.2. Noise introduced during calibration

In order not to introduce additional random noise beyond 0.001 magnitude during image calibration (bias and dark subtraction and at field division) each

calibration image must also satisfy the requirement of 10^6 photoelectrons per pixel. Combined bias, dark, and at field frames are therefore required since 10^6 photoelectrons far exceed the usable well capacity of the CCD. Milli-magnitude precsion from the science frames, on the other hand, can be obtained by binning high-cadence data.

3.3. Noise deriving from atmospheric scintillation

Flux variations stemming from low-frequency atmospheric scintillation are characterized by the following equation (Ryan and Sandler 1998),

$$\frac{\sigma}{\mathrm{S}} = 0.09 \frac{X^{1.5}}{D^{2/3}\sqrt{2\,t}} \exp\left(-\frac{h}{h_0}\right),$$

where $\frac{\sigma}{S}$ is the fractional noise contribution due to atmospheric scintillation, X is the air mass, D is the aperture diameter (in cm), h is the observatory altitude (in km) compared to the atmospheric scale height h_0, and t is the integration time in seconds. Note the same $t^{-1/2}$ dependence as is accumulated with Poisson noise. If 1 milli-magnitude photometric precision is to be obtained, then for stars brighter than $V = 8$ at sea level, scintillation sets the lower exposure time limit at 75s for observations at the zenith ($X = 1.0$), and 250s for observations at distance of 48° from the zenith ($X = 1.5$). In practice, exposure times of 40s produce scintillation values as small as 0.003 mag for a reasonable range of airmass values. (The "Observing Procedures" link at http://www.transitsearch.org contains a scintillation estimator for observation planning.)

3.4. CCD read noise

Using the signal-to-noise formula of Everett and Howell (2001) and neglecting dark current, CCD read noise can approach 1 milli-magnitude for the image scale, seeing, and empirically optimized 8 pixel radius stellar apertures. If, however, stellar apertures are assigned a 20 pixel radius, as experience on a 1 meter telescope at a high altitude site (Castellano 2000) suggests, then read noise approaches 3 milli-magnitudes. Initial data reductions, which used aperture sizes in this range to avoid the detrimental effect of guiding and point spread function variations over the night, resulted in surprisingly poor photometry. We determined that typical amateur-quality CCDs have about 10 times more read noise (15 electrons RMS) than scientific grade CCDs (1 to 2 electrons RMS). Large apertures are thus not a panacea for bright stars when using CCDs with non-negligible read noise. Experiments with a software signal-to-noise calculator and careful entry of CCD parameters in the aperture photometry program revealed this problem during data reductions.

4. Systematic errors

In addition to random noise sources, one must also take care to minimize a variety of potential sources of systematic error. Backside-illuminated and thinned CCDs are

usually best for stellar photometry because they are less affected by intra-pixel sensitivity variations than frontside-illuminated devices (Buffington *et al.* 1991), although frontside devices have achieved precision approaching 1 part in a 100,000 in a laboratory setting (Robinson *et al.* 1995). For frontside-illuminated CCDs, photons must pass through the polysilicon parallel transfer electrodes running in the row direction. These electrodes are used to clock charge out to the serial output registers. These structures are opaque to some wavelengths of visible light and lead to spatial quantum efficiency variations within each pixel. Backside-illuminated devices accept photons directly into the bulk silicon from the "backside" of the CCD where no parallel transfer electrodes are present. Since most amateur-quality CCDs are frontside illuminated, we were keenly aware of the effects of image motion and the resulting effect on photometric precision. Exposures taken without an autoguider resulted in a slow drift of stellar images across the CCD, and the precision of these measurements was uniformly poor.

For CCD differential photometry, differential (or first-order) extinction arises from differences in airmass between the object and comparison stars in a single exposure. Differential extinction increases with airmass. At Lick Observatory, the typical extinction coefficients, a_v, were found to be 0.36 to 0.47 magnitude per airmass in the *V* band (Castellano 2000). We adopt values within this range as typical. In our trial photometry of HD 209458, the maximum angular distance between the object star and the comparison star HIP 108793 was about 12 arc minutes, with HIP 108793 having larger values of airmass. The maximum airmass through which we observed was $X = 1.35$, which results in a maximum predicted differential extinction of 0.002 magnitude. Differential extinction makes the comparison star seem fainter, thereby increasing the difference between it and HD 209458. This produces an upward slope in a differential light curve (as in Figure 5 lower panel) with increasing airmass.

The choice of similar color comparison stars can minimize the second-order extinction which varies with the product of the airmass *X* and the difference $\Delta(B–V)$ in color between the stars. The size of the second-order extinction coefficient is typically 0.03 for $\Delta(B–V) = 1$ over a unit change of airmass (Janes 1996). For our HD 209458 observations, the largest change in air mass over the night was 0.35 and the $\Delta(B–V)$ difference between HD 209458 and HIP 108793 was 0.3 magnitude. This translates to a maximum color-dependent extinction of ~0.0025 magnitude using Janes' estimate of the second-order extinction coefficient of 0.03. Since HD 209458 is the redder star of the pair and is less affected by increasing air mass, second order extinction also makes HIP 108793 seem relatively less bright with increasing airmass, thereby increasing the magnitude difference between the two stars. In our trial observations, second-order extinction also causes an upward slope in the differential light curve with increasing airmass.

5. Instrument description

In order to demonstrate that precise photometry could be achieved with commercial equipment of moderate cost, an amateur-grade telescope and CCD were

obtained. Initial experiments concentrated on obtaining a high-quality transit light curve for HD 209458 "b."

Our telescope was a Meade Instruments Corporation 8-inch aperture LX-200 Schmidt-Cassegrain with an optional equatorial wedge. It was tripod-mounted prior to each observing session. The telescope can be computer controlled and receives positioning feedback signals from a CCD auto-guider. The equatorial wedge was selected to avoid the field rotation inherent with altitude-azimuth telescope systems during a long series of exposures.

Our CCD camera was a Santa Barbara Instrument Group ST-7E camera with a frontside illuminated Kodak KAF-0401E chip of 765×510 pixels of 9 microns size with antiblooming protection (described further below) and an integral autoguider CCD located at the focal plane. This camera has a 16 bit analog-to-digital converter and a gain of 2.3. This choice was partially motivated by HD 209458 "b" transit observations reported in *Sky & Telescope* magazine (Oksanen 2001). For this camera, both CCDs are located beneath the shutter and are cooled thermoelectrically to as much as 25° C below ambient. An integral autoguider was desired as experience has taught us that precise photometry is difficult in the absence of good telescope guiding (Castellano 2000), presumably due to intrapixel sensitivity variations and image motion. Furthermore, focal plane auto-guiding eliminates guide errors that occur with off-axis guiders that suffer from differential exure.

The focal plane location of the guide chip was problematic for obtaining time series data however. This arrangement is better suited for performing long single exposures where the guider is readout frequently while the shutter remains open and an image is acquired with the "science" CCD. In this mode of operation the shutter is closed only when the science CCD is being read out. Guide is then lost until another image is started and the shutter reopens.

For time series photometry, guiding between exposures is as important as (and is perhaps more important than) guiding during exposures; it is the motion of stellar images from frame to frame that leads to brightness variations resulting from pixel sensitivity. The commercial software handles this situation by allowing guiding between science exposures. The user can specify additional delays between exposures that allow the autoguider to reacquire the guide star and re-center it before the next image is begun.

The ST-7E CCD comes in two versions, antiblooming (ABG) and non-antiblooming (NABG). Blooming occurs when the CCD well capacity is exceeded resulting in charge leakage along a column and producing undesirable streaks in images. An antiblooming CCD is useful for CCD photography of faint objects in which a bright star might also be located by chance in the field of view. The antiblooming capability requires a special CCD architecture with insulating channels of polysilicon and additional electrodes along the column directions. These features act as drains for charge that would normally spill out along a column when an individual pixel's well capacity is exceeded (Bui 1991). These charge drains are opaque and reduce the photosensitive area of the CCD, thereby reducing the

quantum efficiency (QE), diminishing the well capacity, and introducing an intentional non-linearity. Reduced QE is not a significant hindrance for photometry of the bright stars found to have planets, but reduced well capacity and non-linearity are definitely problematic.

Anti-blooming reduces the well capacity and introduces non-linearity above a certain fraction of pixel charge well capacity usage. Both of these attributes are undesirable for photometry. Since it was desired to take advantage of the availability of transits of HD 209458 that occurred in the summer of 2001, the only ST-7E CCDs readily available were those with the anti-blooming feature. The CCD manufacturer suggested limiting exposures to use less than half of the pixel well capacity and to determine the linear region of our particular device. It should be noted that the well capacity for the ABG version is already 1/2 the size (50,000 e-) of the non-ABG version (100,000 e-). Limiting exposures to half well capacity results in using only 25,000/2.3 or about 10,000 of the 65535 analog to digital units (ADU) available.

The major challenge in obtaining differential photometry with our off-the-shelf system was to achieve exposures long enough so that the precision of an individual image is not severely scintillation limited. Diminished well capacity certainly doesn't help achieve long exposures. Furthermore, differential photometry between a target star and a comparison star of unequal brightness (which for our application is the usual situation) requires a large dynamic range which is enhanced by deep wells.

A series of exposures were taken with increasing exposure times to test the linearity of the CCD and to establish the linear range of the CCD in ADUs. A plot of exposure time versus integrated flux summed over an aperture for HD 209458 is shown as the upper panel in Figure 2. The lower panel of Figure 2 plots the deviation from a straight line, and indicates that exposure times as long as 4 seconds (for these conditions) result in non-linearity of less than 1 percent. We, therefore, fixed exposure times conservatively at 2 seconds. The error bars in the lower panel of Figure 2 are due almost entirely to scintillation (Young 1974; Ryan and Sandler 1998) for these short exposures.

A feature of the commercial image analysis software that determines the maximum pixel value was used to produce the upper panel of Figure 3. The short dashed line near 22000 ADUs is the CCD pixel well capacity translated into ADUs by dividing by the gain. Similarly, the long dashed line near 11,000 ADUs is half the CCD pixel well capacity (the working region for photometry recommended by the manufacturer) translated into ADUs by dividing by the gain. This plot of exposure time versus maximum pixel value clearly shows the effects of well capacity at 50000/ 2.3 = 21739 ADUs where increasing the exposure time does increase the flux summed over an aperture (Figure 2) but not the maximum pixel value (Figure 3). We take this to mean that at least one pixel within the photometric aperture had saturated.

The upper panel of Figure 3 shows that the maximum pixel within the stellar aperture approaches half the well capacity near an exposure time of 2 seconds and is approaching the full well capacity near an exposure time of 4 seconds. The lower panel of Figure 3 is a plot of the difference in magnitude of HD 209458 and HIP 108793.

For a linear system the difference in brightness of two stars should not depend on the exposure time. The lower panel of Figure 3 shows non-linearity clearly beyond an exposure time of 4 seconds where significant departures from a horizontal line are seen. This non-linearity is best explained by a diminished response for the brighter star of the pair (HD 209458) while the dimmer star (HIP 108793) remains linear, resulting in the difference between the two becoming smaller with longer exposure time (towards smaller negative values of differential magnitude).

Based on this experiment, ADU values were limited to less than 10,000 (which corresponds to 23,000 electrons, or about roughly the half the well capacity of 50,000 electrons for this antiblooming CCD).

6. The observing procedure for recording a transit

The series of images that served as the basis for the differential light curve of HD 209458 were obtained with the autoguider in operation between exposures. This was necessary because the exposure times required to avoid saturation (2s) were short enough that autoguider performance was poor because of the significant atmospheric image motion that occurs on these time-scales. A delay of 10 seconds was needed between exposures for the autoguider to have time to re-acquire and re-center the guide star. The performance under this scenario is illustrated by Figure 4, where the row and column positions of HD 209458 and the comparison star HIP 108793 are plotted versus time. Motion over the night was less than 5 pixels.

After initial experiments with the telescope a focal reducer was added to increase the FOV. With the focal reducer attached to the telescope rear cell, a T-adapter ring and a 15 mm T-thread adapter attached to the camera, an effective focal ratio of F/3.3 was achieved (as stated by the manufacturer for this configuration). This allowed the selection of a suitably bright comparison star (HIP 108793) and resulted in a field of view nearly one-half degree in the long dimension.

Our CCD frame readout rate is 30 KHz; 13 seconds are thus required to read out the CCD's 390,015 pixels. Since this is long compared to the typical unfiltered integration time possible before saturation occurs (a few seconds at most), a very low observing efficiency results. An attractive refinement for future observations would be to use some means to increase the exposure time (a deliberate defocus, for example, or insertion of a narrow band or neutral density filter) so that each exposure is longer for a given total flux level (limited by the CCD well capacity) and hence less affected by scintillation. A 10 or 20 fold increase in exposure time should be possible before Poisson noise becomes the limiting factor.

For our observing conditions, short exposures and long readouts limited us to 40 seconds of open shutter time in each 12 minute binning interval. Even with 40 seconds of open shutter time, the photometry is scintillation-limited to a best possible precision of about 3 millimags (Figure 1). With a broadband filter or defocus to allow 40 second exposures in the linear regime, we might have been able to produce one 0.003 mag precision exposure per minute and the further averaging of these

finely cadenced samples could potentially have achieved ~1 milli-magnitude precision for bins of 12-minute duration.

Since transit observations are time-critical in nature, the telescope was typically set up one night before a predicted transit, and the following procedures executed to ensure that (1) the equipment functioned as expected, (2) no horizon limitations were encountered during the session, and (3) the observer is re-acquainted with the hardware and software.

The telescope was mounted on the equatorial wedge and tripod as was roughly aligned with the north celestial pole, and the telescope, computer, and camera were powered on. The camera temperature was set at 25° C below ambient and allowed to cool. The focal reducer and camera were fitted to the telescope, a directory for image storage was created, file prefixes and formats (FITS) were specified, and a test exposure was taken to verify storage. Next, communication between the telescope and the telescope pointing program was established. Flat fields of the sky were taken at dusk at the value of focus determined from the previous night's observing. The telescope hand controller was used to move the telescope by a small amount between at field exposures, thus allowing the removal of stars from the combined flat field.

As soon as Polaris was visible, the telescope was aligned in equatorial mode using the procedure outlined by the manufacturer. Because of a mechanical interference between the camera body and the telescope fork mount near the pole, this required removal of the CCD and centering an unfocused image of Polaris on the cross hairs of a reticle eyepiece.

Telescope alignment was completed using the bright star recommended by the internal telescope alignment software (usually Vega), the star was centered on the now re-installed CCD by manually slewing with the hand controller and the alignment completed. The telescope was manually slewed to a bright star near HD 209458. Thereafter, all telescope pointing was done with the computer. The telescope was then slewed to HD 2094558 (by selecting it on the computer screen) and the focus was refined. The autoguider was then calibrated using HD 209458. The FOV was offset until HD 209458 and HIP 108793 were nearly equally displaced from the image center. Further fine adjustments were made until a suitable guide star was located on the autoguider CCD.

The above procedures were typically completed within a half-hour of sunset, and the imaging session was begun. The autoguider was enabled with 5 second autoguider integrations during the forced 10 second delays between the 2 second science exposures. The CCD readout time of about 13 seconds, the image download time, and the forced 10 second delay between images required for good guiding resulted in 20 images every ~12 minutes or about 1 per ~35 seconds. Frequent monitoring of the peak flux within a single pixel was required to insure operation in the linear region of the CCD. At the conclusion of the evening's observing, a series of 10 bias and 10 dark frames was taken.

7. Data reductions

Once the images and calibration frames were saved to disk in FITS format, a reduction group was composed for the commercial image reduction software. This involved simply placing the bias, dark and flat field frames in directories and naming them appropriately. As mentioned above, Poisson statistics require 10^6 photoelectrons per pixel in the flat field frames in order to achieve a final photometric precision of 0.001 magnitude. In practice, a less stringent requirement applies, because the flux from each star is spread over an aperture no smaller than 8 pixels in radius (an area of ~200 pixels).

To achieve this aim, ten of each type of calibration frame were obtained and averaged together (using a statistics utility included with the commercial software) to produce combined master bias, dark and flat field frames. Flat fields typically contained of order 3600 ADUs in the maximum pixel and ~10% vignetting towards the field edges. The averaged flux in the combined flat field summed over a 200 pixel stellar aperture was thus 7.2×10^6 photoelectrons, resulting in a Poisson noise error contribution of less than 0.001 magnitude in the flat fields.

Calibration of the several hundred obtained images took about an hour of computer time. The raw uncalibrated images were saved for comparison purposes to ensure that the calibration process did not degrade the photometric precision.

A selection of 50 images were loaded and reviewed. After the quality of the individual images was verified, the object and comparison star were selected, aperture sizes were chosen and the read noise and CCD gain were specified. This last step is crucial in order to ensure good error estimates, which in turn are critical for proper aperture size selections to maximize photometric precision. Once apertures were selected, software would then identify the object and comparison star in all images in the series, determine their centroids, apply the apertures, determine the net flux and background level, and output the results to a text table. Aperture sizes were optimized by minimizing the estimated errors produced by the photometry software, and minimizing the RMS scatter (as evidenced by a calculation of the standard deviation) of a portion of the reduced light curve.

The table of results was imported into a spreadsheet and differential magnitudes were formed by taking the ratio of the flux of HD 209458 to HIP 108793 and converting to the magnitude system, averaging was performed, and a light curve plot was produced.

8. Results

The ability to perform simple two-star differential photometry with the commercial software allowed almost real time examination of the raw images (not bias and dark subtracted or flat field divided) to assess the quality of the night's photometry. Examining one half hour of data (60 images and averaging them by 10) revealed that the standard deviation of the data was less than 1 percent. This was invaluable in

being able to immediately verify telescope and CCD performance and the quality of the night's observing conditions.

Figure 5 illustrates the quality of the photometric data obtained for the transit observation of HD 209458 from the night of October 19, 2001. These plots were produced using an IDL program that read the tabular output of the photometry software and are based on the same data as Figure 1 of Seagroves *et al.* (2003). The detailed examination of all the available information that a flexible data analysis package allows was invaluable in refining the observing and data reduction techniques. It is not expected that the typical amateur observer will have this facility or interest in the data at this level of detail. The goal of this detailed analysis was to understand the noise sources and eliminate them through refined observing procedures rather than during data reduction. Stated another way, the goal was to produce observational procedures that result in sufficient signal to noise and control of systematic errors so that transits are immediately visible in a light curve produced at the telescope.

9. Further improvements

After using the equipment to the obtain proof-of-concept photometric light curve shown in Figure 5, we upgraded the observatory for remote control, and located it to a small robotic telescope dome that provides automatic slit tracking of the telescope pointing position, and remote opening and closing of the slit. A CCD universal serial bus (USB) webcam was installed on the finder scope to allow the "synch" procedure for aligning the telescope each night to be performed remotely. Polar alignment was refined over several nights using the drift method. Once the alignment is acceptable and if the CCD remains installed, it is possible for flat field frames to be reused over many nights, as the CCD focus was found to be very stable. We also installed an SBIG CFW-8 5-position filter wheel fitted with blue, green, red and clear interference filters. The filter passbands are listed in Table 1. These filters are an effective low-cost alternative to the standard Johnson *UBVRI* set.

Table 1. SBIG color filter passbands.

Color	*Passband (Angstroms)*
Blue	3920–5080
Green	4880–5740
Red	6120–6700

Fitting the filter wheel to the front of the CCD housing increased the distance between the focal reducer and the CCD, resulting in an effective focal ratio reduction to F/2.6 (measured) from the F/3.3 estimated in Section 6. This F/ratio resulted in a FOV about 1/2 degree by 2/3 of a degree. The larger FOV made the selection of comparison stars easier, but the shorter focal length led to less than optimal pixel

sampling, increased vignetting and degraded image quality toward the edges of the field. This was especially true at the location of the autoguider some half a degree from the imager field center.

The observatory computer had the usual suite of software installed including MIRA, The Sky, CCDSoft, Digital Dome Works (for dome control), and Robofocus, along with an Internet connection. A remote access program allowed remote control of the observatory computer and image file transfer. The dome has its own weather station that allows unattended observing; the dome slit will shut automatically if weather conditions exceed programmed limits. At the end of a night of observing data were written to a single CD-ROM. The effective stellar profile FWHM (a combination of seeing and telescope vibration) was typically 8–10 arcseconds.

10. Photometric observations of GJ 876

GJ 876 is a nearby red dwarf star (spectral type M4) with $V = 10.17$, an estimated mass of $M = 0.32M_{\odot}$, and an estimated radius of $0.3R_{\odot}$ (Marcy *et al.* 1998). It is accompanied by two planets: GJ 876 "b," with $P \sim 60$d, $M\sin(i) = 1.9M_{JUP}$, and GJ 876 "c," with $P \sim 30$d, $M\sin(i) = 0.6M_{JUP}$ (Marcy *et al.* 1998, 2001). The planets are participating in a 2:1 mean motion resonance, and exhibit significant planet-planet interactions on timescales of only a few years. The interactions are strong enough that they must be included in the orbital model fit to the observed radial velocities of the star(Laughlin and Chambers 2001).

Dynamical fits to the GJ 876 planetary system by Laughlin and Chambers (2001) weakly favor a co-planar configuration which is inclined by roughly 40° to the plane of the sky. In this case, no transits would be observable. Astrometric evidence presented by Benedict *et al.* (2003), on the other hand, suggests that the inclination of the outer planet is close to 90° (i.e. edge-on). It is thus important to verify whether or not the planets are transiting. This task is made easier for the GJ 876 planets, whose large size relative to the small parent star should lead to a central transit depth of more than 10%.

Since GJ 876 is several magnitudes fainter than HD 209458, observations are less affected by scintillation arising from short exposures. Furthermore, at $V = 10$, comparison stars of equal apparent magnitude should be about 5 times as common as at 8th magnitude (Allen 1976), and this is indeed the case. GJ 876 is flanked by several suitably bright comparison stars, and longer exposure times can be tolerated without risking CCD saturation and nonlinearity. This improvement over HD 209458 bodes well for the future of photometric transit searches with small telescopes as RV surveys proceed to fainter target stars. The spectral type of GJ 876 (HIP 113020) is M4 and the star is quite red ($B–V = 1.60$). Exposures of 90 seconds' duration with the "red" filter were chosen.

GJ 876 was observed on the night of November 26, 2003, following an unsuccessful attempt on July 28, 2003. Our dynamical model of the GJ 876 system indicates that a possible transit window for GJ 876 "c" (the inner planet) occured between

JD 2425270.21 and JD 2425270.72. The estimated width of this transit window includes both the 0.125-day duration predicted for a central transit and also the one-sigma estimated uncertainty in the predicted time of central transit obtained via a Monte-Carlo analysis of synthetic data sets (Laughlin *et al.* 2004). The field was acquired within an hour of sunset when GJ 876 was near the meridian (at an airmass X ~1.6) and was observed for nearly 5 hours until the airmass approached a value X ~5. The night was not cloud-free. An 80% drop in flux from GJ 876 and the comparison star was observed for about a half-hour near JD 2452970.68.

Data reductions were performed as described in Section 7, resulting in the light curve shown in Figure 6 and an estimated precision of 1 to 2 percent for individual differential measurements over the entire data set. For the more than 2 hours of data taken at an airmass of less than 2, the photometric precision of the average of 10 measurements was as small as 0.003 magnitude. This level of precision is close to what would be expected for scintillation noise alone for these conditions. An upward trend in brightness of GJ 876 relative to the comparison star (HIP 112920, V = 9.74, G3V, B–V = 0.51) of about 1% is seen towards the end of the observations. This trend is consistent with the expected brightening of a red object star relative to a bluer comparison star due to color dependent extinction as high values of airmass are reached.

The observed lack of a transit allows us to partially constrain the orbital configuration of the GJ 876 planets beyond what is currently possible using radial velocity data alone. Our photometric light curve indicates that no planetary transit of the expected ~10% depth occured during the time epoch spanning JD 2452970.58 to JD 2452970.77, which eliminates part of the nominal JD 2452970.21–JD 2452970.72 transit window from consideration.

11. Conclusion

Our results show that sufficient signal-to-noise and sampling can be obtained with a telescope/CCD/software system common to many amateur astronomers so that the confirmation and detection of transits of Jupiter-sized extrasolar planets around sun-like stars is possible. In addition, excellent results can be obtained under non-ideal observing conditions, including thin clouds, exposure times limited by CCD non-linearity, short exposures leading to significant scintillation, and less-than-perfect telescope guiding performance, among others. Refinement of the technique from this beginning is certainly possible and we look forward to continuing to work with amateur astronomers and learning of the many innovations and improvements made by our collaborators as they search for additional transits with small telescopes and commercial CCDs in their backyards.

TC wishes to thank NASA Ames Chief Scientist Dr. Stephanie Langhoff and the NASA Ames Director's Discretionary Fund for their continued support. GL was supported by a Faculty Small Research Grant at Santa Cruz. SH and GS would like to thank the National Science Foundation Research Experience for Undergraduates

program. DB and RR would like to thank the National Association for Equal Opportunity in Higher Education for their summer support.

We thank Jay Strader and Justin Lacy for observing assistance and advice.

References

Allen, C. W. 1976, *Astrophysical Quantities*, Athlone P., London.

Benedict, G. F., McArthur, B. E., and Nelan, E. P. 2003, *Am. Astron. Soc. Meeting 203*, 67.05.

Brown, T., Charbonneau, D., Gilliland, R., Burrows, A., and Noyes, R.W. 2001, *Astrophys. J.*, **552**, 699.

Buffington, A., Booth, C.H., and Hudson, H.S. 1991, *Publ. Astron. Soc. Pacific*, **103**, 685.

Bui, C. 1991, *CCD Astronomy*, Willmann-Bell, Richmond.

Castellano, T. 2000, *Publ. Astron. Soc. Pacific*, **112**, 821.

Charbonneau, D., Brown, T. M., Latham, D. W., and Mayor, M. 2000, *Astrophys. J. Lett. Ed.*, **529**, L45.

Charbonneau, D. 2004, "A Review of the Current Status of Follow-Up Techniques to Study Known Extrasolar Planets," Astrophysics Abstract astro-ph 0312252, http://arxiv.org/abs/astro-ph/0312252, to appear in Astron. Soc. Pacific Conf. Ser. IAU Symp. 219: *Stars as Suns: Activity, Evolution, and Planets*, eds. A. O. Benz and A. K. Dupree.

Cody, A. M., and Sasselov, D. D. 2002, *Astrophys. J.*, **569**, 451.

Everett, M. E., and Howell, S. B. 2001, *Publ. Astron. Soc. Pacific*, **113**, 1428.

Gilliland, R. L., Brown, T. M., Duncan, D. K., Suntzeff, N. B., Lockwood, G. W., Thompson, D. T., Schild, R. E., Jeffrey, W. A., and Penprase, B. E. 1991, *Astron. J.*, **101**, 541.

Henden, A. A., and Kaitchuk, R. H. 1990, *Astronomical Photometry*, Wilmann-Bell, Richmond.

Henry, G. W., Marcy, G. W., Butler, R. P., and Vogt, S. S. 2000, *Astrophys. J. Lett. Ed.*, **529**, L41.

Janes, K. 1996, J. Geophys. Res., 101, E6, 14853.

Konacki, M., Torres, G., Sasselov, D., and Jha, S. 2003 *Astrophys. J.*, **597**, 1076.

Laughlin, G., and Chambers J. E., 2001, *Astrophys. J. Lett. Ed.*, **551**, L109.

Laughlin, G. *et al.* 2004, in preparation.

Marcy, G., Butler, P., Vogt, S., Fischer, D., and Lissauer, J., 1998, *Astrophys. J. Lett. Ed.*, **505**, L147.

Marcy, G., Butler, P., Vogt, S., Fischer, D. Lissauer, J., and Rivera, E. 2001, *Astrophys. J.*, **556**, 296.

Mazeh, T., Naef, D., Torres, G., Latham, D. W., Mayor, M. M., Beuzit, J.-L., Brown, T. M., Buchhave, L., Burnet, M., Carney, B. W., Charbonneau, D., Drukier, G. A., Laird, J. B., Pepe, F., Perrier, C., Queloz, D., Santos, N. C., Sivan, J.-P., Udry, S., and Zucker, S. 2000, *Astrophys. J. Lett. Ed.*, **532**, L55.

Oksanen, A. 2001, *Sky & Telescope*, **101**, 1, 14.

Pepper, J., Gould, A., and Depoy, D. L. 2003, *Acta Astron.*, **53**, 213.
Robinson, L. B., Wei, M. Z., Borucki, W. J., Dunham, E. W., Ford, C. H., and Granados, A. F. 1995, *Publ. Astron. Soc. Pacific*, **107**, 1094.
Ryan, P., and Sandler, D. 1998, *Publ. Astron. Soc. Pacific*, **110**, 1235.
Seagroves, S., Harker, J., Laughlin, G., Lacy, J., and Castellano, T. 2003, *Publ. Astron. Soc. Pacific*, **115**, 1355.
Wittenmyer, T. 2003, Master's Thesis, Univ. Calif. San Diego.
Young, A. T. 1974, *Methods of Experimental Physics: Vol. 12A, Astrophysics, Optical and Infrared*, Academic P., New York.

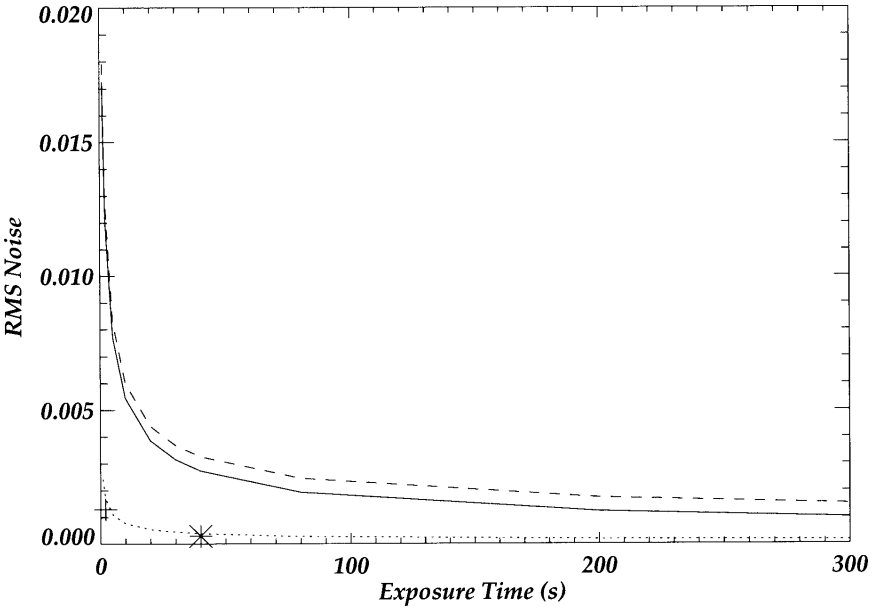

Figure 1. RMS noise versus open shutter time in seconds for the major random noise sources. Scintillation for a 20 centimeter aperture telescope, at sea level and an air mass of X = 1.0 is plotted as a solid line. Poisson noise is plotted as a dotted line for an 8th magnitude star. The total noise is plotted as a dashed line and is displaced upward slightly to allow it to be distinguished from the scintillation component alone. Read noise for the apertures size selected (8 pixels radius) is plotted as a "plus" sign for a single exposure of 2 seconds total duration, and as an "asterisk" for an exposure of 40 second total duration.

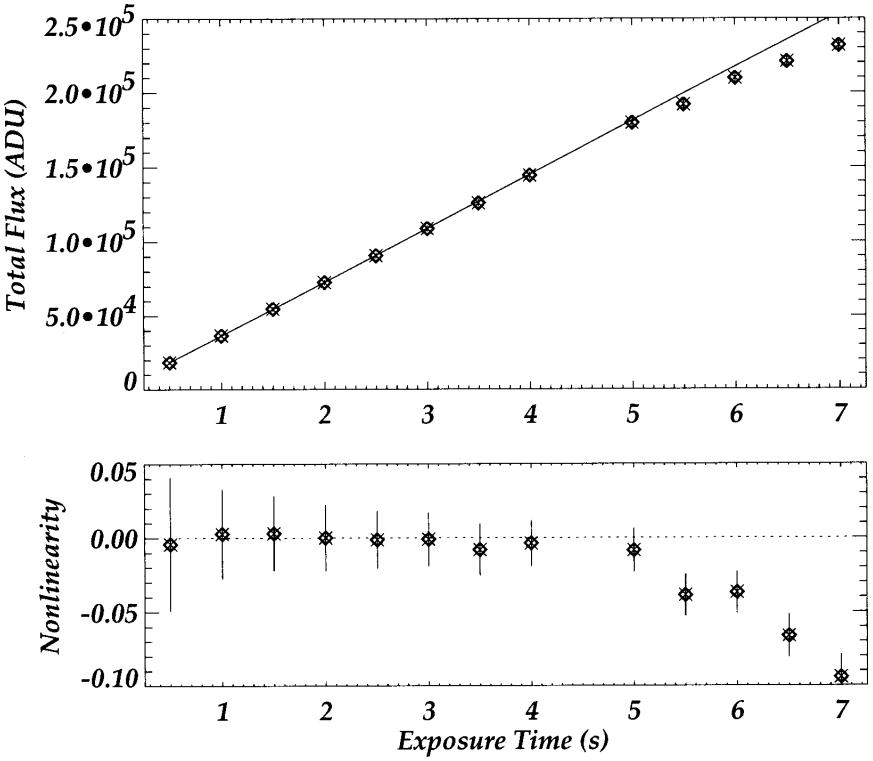

Figure 2. Upper panel: Flux summed over an aperture plotted versus exposure time compared to the best fit straight line determined using the IDL routine LINFIT to the first 5 points. Note the deviation from linearity for exposure times beyond 5 seconds. Lower panel: Size of the departure from linearity obtained by subtracting the best fit line from the individual measurements. Exposure times longer than 4 seconds should certainly be avoided for these conditions. The error bars are due to scintillation alone.

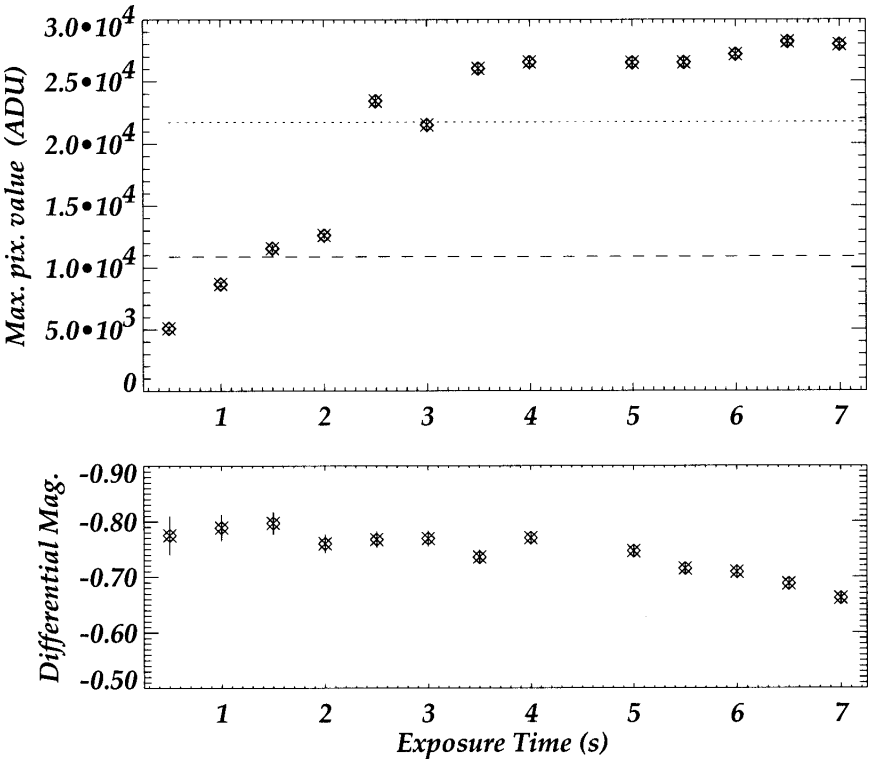

Figure 3. Upper panel: Maximum pixel value (in ADUs) within the stellar aperture versus exposure time. The short dashed line near 22,000 ADUs is the CCD pixel well capacity translated into ADUs by dividing by the gain. Similarly, the long dashed line near 11,000 ADUs is half the CCD pixel well capacity (the working region for photometry recommended by the manufacturer) translated into ADUs by dividing by the gain. This plot of exposure time versus maximum pixel value and Figure 2 clearly show the effects of well capacity at 50000/2.3 = 21739 ADUs where increasing the exposure time does increase the flux summed over an aperture (Figure 2) but not the maximum pixel value. The error bars are smaller than the symbols that represent the data for all but the shortest exposures. Lower panel: differential magnitude of HD 209458 and HIP 108793 plotted versus exposure time and showing the effect of saturation. For a linear system the difference in brightness of two stars should not depend on the exposure time. The effect of non-linearity is clearly seen beyond an exposure time of 4 seconds where significant departures from a horizontal line are seen. The uncertainties in the ADU values for the maximum pixel in the upper panel are due to Poisson noise alone while the uncertainties in the differential magnitudes for the lower panel are the root mean square sum of scintillation and read noise. Poisson noise, sky and dark current are minor contributors to the total noise for this panel.

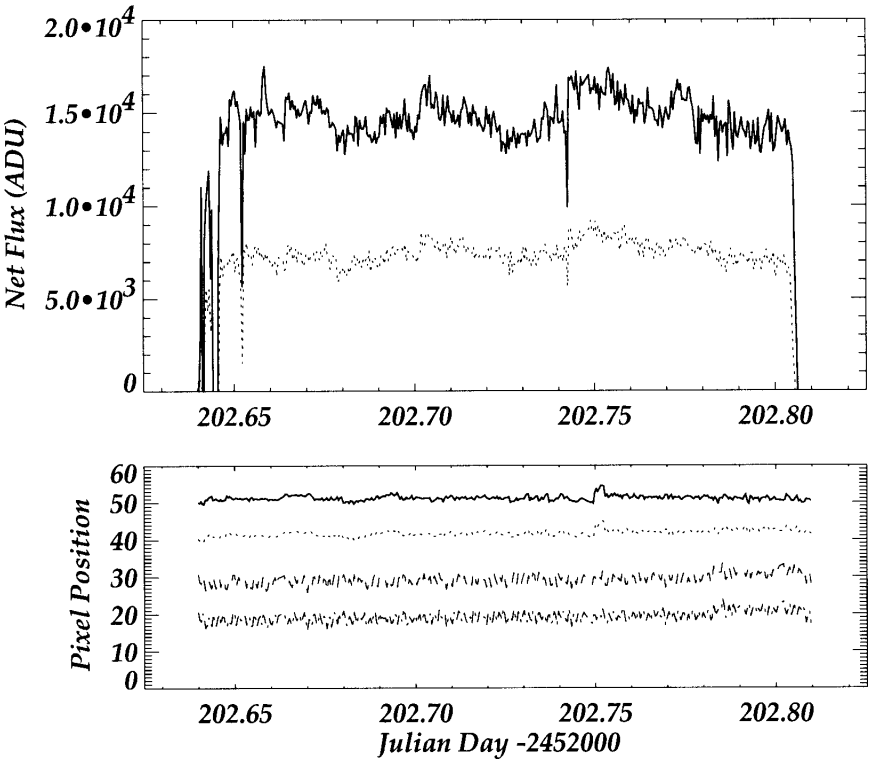

Figure 4. Two diagnostics of data quality useful for assessing the potential of systematic effects for producing a spurious transit-like trend. Upper panel: Raw brightness of HD 209458 and HIP 108793 versus time, showing the effects of significant cloud early in the evening and light variable cloud in the middle of the observation producing about a 10 percent drop in total flux. The setting of the field behind a structure caused a significant drop in brightness near JD 2452202.8, resulting in a few spurious measurements which were discarded. Also note the sudden drop in brightness for both stars near JD 2452202.75, this was due to condensation on the telescope corrector plate, a condition rectified with a hair dryer. Lower panel: Row and column positions of the two stars as a function of time. In order, from top to bottom, are the row positions of stars 0 and 1, and the column positions of stars 0 and 1. All have arbitrary pixel position offsets subtracted so that they may be shown on a common scale. Note the short term variations in position with amplitudes of about 5 pixels with greater movement in the column (east-west or tracking) direction. A slow drift towards larger row and column values is also seen for both stars. A sudden change in positions for both stars near JD 2452202.75 was due to condensation on the telescope corrector plate (described above); autoguiding continued during this episode and the photometry didn't suffer appreciably.

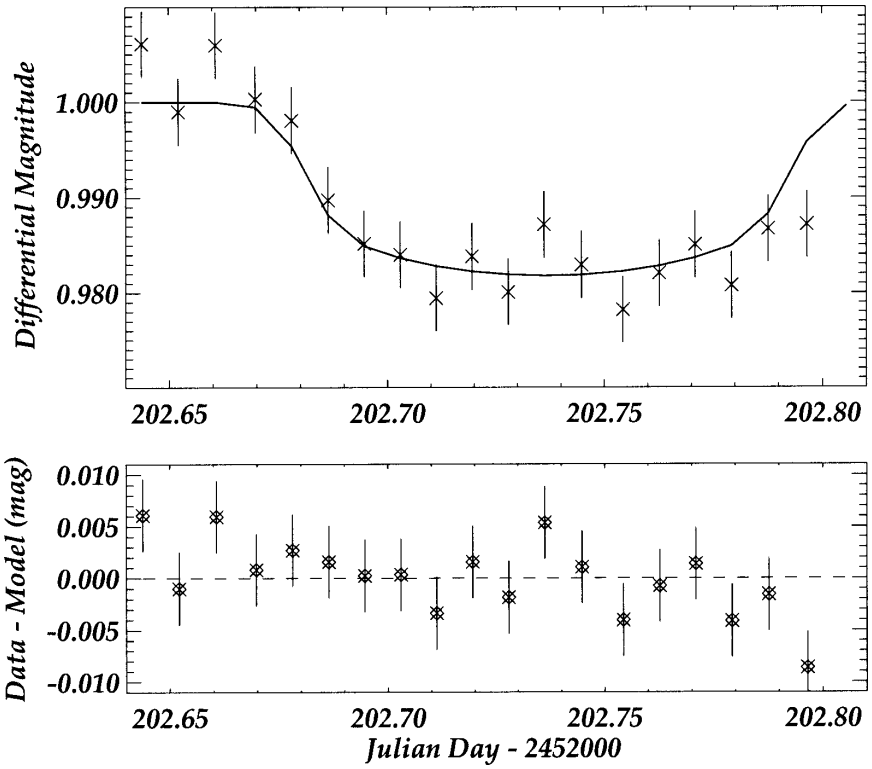

Figure 5. Upper panel: photometric data obtained during the observation of the transit of HD 209458 on the night of October 19, 2001, with the telescope/CCD described in a suburban backyard. The data was flux normalized and averaged over 20 measurements (points with error bars) and are compared to a limb-darkened transit model using the planet and star parameters obtained by Brown *et al.* (2001) (solid line). Arbitrary offsets in the horizontal and vertical scales were applied to minimize the RMS differences between the data and the model. The error bars are 0.0035 magnitude and are estimated values for scintillation for the combined exposure time of 40 seconds. A single data point at the end of the time series is off scale. This datum (composed of the average of 20 measurements) was corrupted by the setting of the field behind a building and a dramatic loss of flux (seen near JD 2452202.8 in the lower panel of Figure 4). Lower panel: Difference between the data and the model. The RMS deviation for this night was 0.003 magnitude. The increase in scatter towards the end of the transit can be explained by the increasing air mass and associated scintillation towards the end of the observing session. There may also be a linear trend toward more negative values of about 0.5 to 1 percent. This could be due to differential and color-dependent extinction, which contribute, respectively, a calculated 0.003 and 0.002 magnitude in the same direction as the trend observed for these observing conditions.

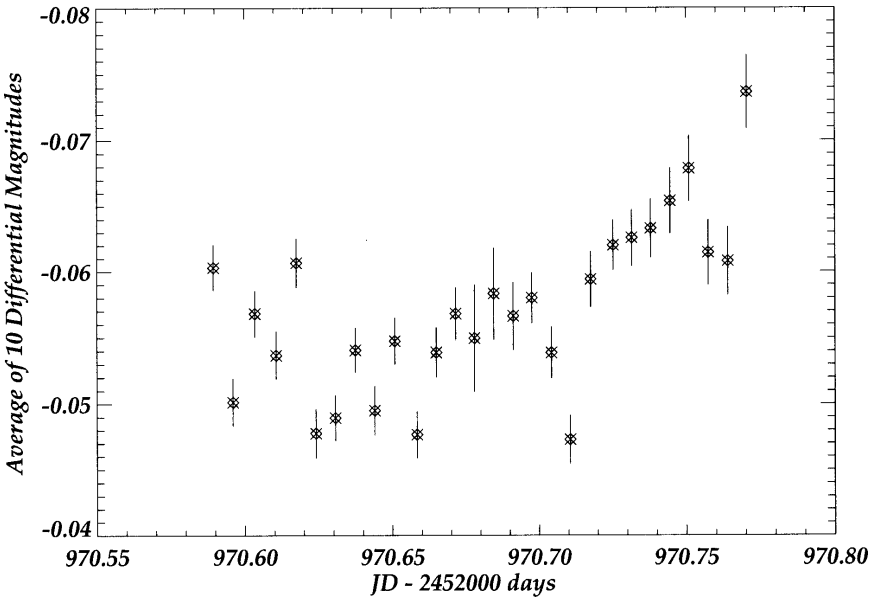

Figure 6. Differential light curve obtained for GJ 876 on the night of November 26, 2003, using the Transitsearch.org rooftop observatory at NASA Ames Research Center. The differential brightness of the average of 5 measurements between GJ 876 and the comparison star HIP 112920 is shown. The large error bars near fractional Julian day 0.68 are due to a significant drop in flux presumably due to cloud cover. The slow upward trend at the end of the dataset is easily explained as color-dependent extinction. No evidence for a 10 percent transit signal is seen.